Rapid Communications

Local polarization in oxygen-deficient $LaMnO_3$ induced by charge localization in the Jahn-Teller distorted structure

Chiara Ricca,[1,2] Nicolas Niederhauser,[1,*] and Ulrich Aschauer[1,2,*]

[1]*Department of Chemistry and Biochemistry, University of Bern, Freiestrasse 3, CH-3012 Bern, Switzerland*

[2]*National Centre for Computational Design and Discovery of Novel Materials (MARVEL), Switzerland*

(Received 8 March 2020; revised 21 October 2020; accepted 25 November 2020; published 10 December 2020)

The functional properties of transition metal perovskite oxides are known to result from a complex interplay of magnetism, polarization, strain, and stoichiometry. Here, we show that for materials with a cooperative Jahn-Teller distortion, such as $LaMnO_3$ (LMO), the orbital order can also couple to the defect chemistry and induce novel material properties. At low temperatures, LMO exhibits a strong Jahn-Teller distortion that splits the e_g orbitals of the high-spin Mn^{3+} ions and leads to alternating long, short, and intermediate Mn-O bonds. Our DFT+U calculations show that, as a result of this orbital order, the charge localization in LMO upon oxygen vacancy formation differs from other manganites, such as $SrMnO_3$, where the two extra electrons reduce the two Mn sites adjacent to the vacancy. In LMO, relaxations around the defect depend on which type of Mn-O bond is broken, affecting the d-orbital energies and leading to asymmetric and hence polar excess-electron localization with respect to the vacancy. Moreover, we show that the Mn-O bond lengths, the orbital order, and consequently the charge localization and polarity are tunable via strain.

DOI: 10.1103/PhysRevResearch.2.042040

The family of doped (La,Ca/Sr)MnO_3 perovskite manganites has attracted great interest due to its very rich phase diagram and its unusual functional properties (colossal magnetoresistance [1–5], photoinduced infrared absorption [6], and efficient hole conductivity [7]) with strong potential for new applications in the fields of electronics, spintronics, and energy conversion. The orbital order plays a significant role in determining these properties and is strongly coupled with the other electronic, structural, and spin degrees of freedom [8,9]. $LaMnO_3$ (LMO) as the end member of this family also exhibits interesting properties such as a pressure-induced insulator-to-metal transition [10] and a dielectric anomaly [11], that also depend on the orbital order [12,13].

Below 750 K, LMO adopts a distorted orthorhombic (*Pbnm*) perovskite structure [see Fig. 1(a)] with an *A*-type antiferromagnetic order (*A*-AFM, Néel temperature $T_N \approx$ 140 K [14]), with Mn atoms coupled ferromagnetically in the *ac* plane and antiferromagnetically along the *b* axis [15–17]. The stabilization of this orbital-ordered insulating state is a consequence of the high-spin Mn^{3+} ($t_{2g}^3 e_g^1$) ions inducing a strong cooperative Jahn-Teller (JT) distortion that splits the e_g orbitals ($d_{z^2}/d_{x^2-y^2}$ orbitals are alternately occupied within the orthorhombic *ac* plane) and lead to alternating long and short in-plane Mn-O bonds, along with intermediate bonds along

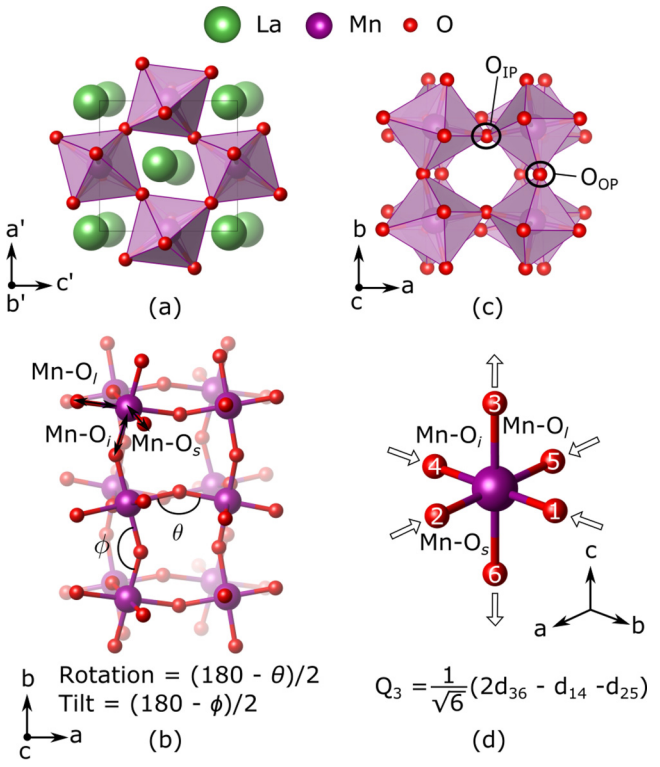

FIG. 1. (a) *Pbnm* unit cell of *A*-AFM $LaMnO_3$ (LMO). (b) Definition of the rotation and tilt angles and of the short (Mn-O_s), intermediate (Mn-O_i), and long (Mn-O_l) Mn-O bonds. (c) The (2 × 2 × 2) LMO supercell used in this work with the two inequivalent V_O positions: in the *ac* plane (IP) and perpendicular to it (OP). (d) Definition of the Jahn-Teller distortion amplitude Q_3: d_{36}, d_{14}, and d_{25} are distances between the corresponding O atoms. Axes a', b', and c' are orthorhombic, while a, b, and c are pseudocubic.

*ulrich.aschauer@dcb.unibe.ch

the b axis [see Fig. 1(b)]. There are two symmetry-distinct oxygen atoms in this structure: the in-plane O (O_{IP}) in the ac plane with one short and one long Mn-O bond, and the out-of-plane O (O_{OP}) along the b direction with two intermediate Mn-O bonds [see Fig. 1(c)].

Unlike most other perovskite oxides, bulk LMO can exhibit oxygen superstoichiometry ($LaMnO_{3+\delta}$), which is accommodated through cation vacancies rather than oxygen interstitials [18–21]. $LaMnO_{3+\delta}$ has an extremely complex magnetic phase diagram exhibiting paramagnetic, ferromagnetic (FM), and canted AFM order as well as a spin-glass state as a function of temperature and O superstoichiometry [19]. Topotactic low-temperature reactions [22,23] were shown to lead to oxygen substoichiometric $LaMnO_{3-\delta}$ with oxygen vacancies (V_O), where for $0.00 \leqslant \delta \leqslant 0.20$, the A-AFM order persists below $T_N \approx 140$ K [23]. The FM behavior often observed in LMO thin films [24–31] was explained by Mn^{3+}-Mn^{4+} double exchange due to the cation deficiency generally observed in these films. It was suggested that, below a critical thickness of 6 unit cells, LMO thin films become AFM [32], but several authors also reported thicker films with bulklike AFM behavior obtained either through growth [33,34] or high-temperature annealing [35] under conditions favoring the formation of V_O.

In this Rapid Communication we investigate strained stoichiometric and oxygen-deficient LMO by density functional theory (DFT) calculations within the QUANTUM ESPRESSO package [36,37] (see Supplemental Material [38] Sec. S1 for details). At the PBEsol+U [39,40] level of theory with a self-consistently computed Hubbard U for Mn-3d states [41,42], we correctly describe the JT distorted structure, which is crucial to accurately predict magnetic and electronic properties [13,43–45]. As can be seen from Supplemental Material [38] Table S3, not only are the computed lattice parameters in good agreement with experiment (relative error below 1%), but we also obtain a good description of the JT distortion (quantified via the magnitude of the Q_3 mode [see Fig. 1(d)]) and reproduce the Mn-O bond lengths to within 2% of experiment. We find the orbitally ordered insulating (see Supplemental Material [38] Fig. S1) state with $d_{z^2}/d_{x^2-y^2}$ orbitals being alternately occupied within the orthorhombic ac plane, which is consistent with the alternating Mn-O_s and Mn-O_l bonds. The direct gap of about 1 eV is in good agreement with experiments, while the indirect gap of 0.69 eV is lower than reported in previous theoretical studies [13,43], but still larger than experiment [46].

Under experimentally relevant conditions, i.e., in the oxygen-poor limit and for a Fermi energy close to the experimental indirect band gap of 0.24 eV [46], the singly charged oxygen vacancy ($V_O^\bullet$ in Kröger-Vink notation [47]) is the favored charge state for V_O in bulk LMO (see Fig. 2), the neutral defect ($V_O^{\bullet\bullet}$) being less stable by about 0.2 eV. However, already for 0% strain, corresponding to a cubic substrate with the same ac area as bulk LMO, epitaxial strain renders $V_O^{\bullet\bullet}$ and $V_O^\bullet$ formation energies nearly degenerate, the neutral defect being further stabilized under compressive strain, as we will discuss in more detail later. For these reasons and being mainly interested in $LaMnO_{3-\delta}$ thin film properties, we consider here only neutral oxygen vacancies, for simplicity referring to them as V_O in the following. Singly ($V_O^\bullet$) and doubly charged (V_O^X) vacancies are described in Supplemental Material [38] Secs. S5 and S6.

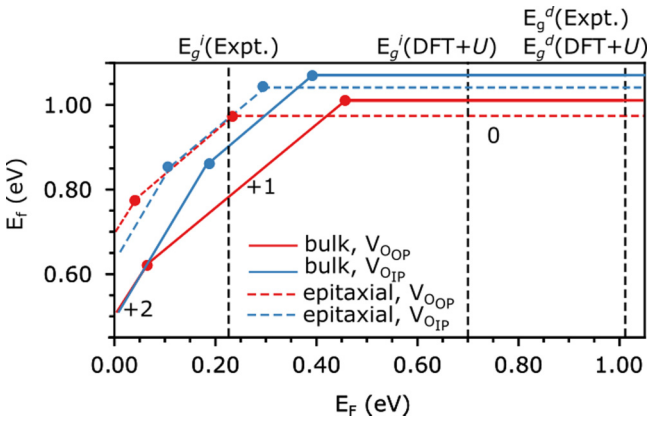

FIG. 2. Oxygen vacancy formation energy (E_f) in bulk LMO and for 0% epitaxial strain under oxygen-poor conditions ($\Delta\mu_O = -2.21$ eV) and in different charge states computed as a function of the Fermi energy (E_F) with respect to the valence band maximum of stoichiometric LMO. Only the most stable charge state is reported as indicated next to each line. The vertical dashed lines indicate E_F values corresponding to the experimental and theoretical direct and indirect band gaps (see Supplemental Material [38] Table S3).

Upon neutral oxygen-vacancy formation, the JT distorted structure leads to excess charge localization different from that observed, for example, in $CaMnO_3$ and $SrMnO_3$ [42,48], where the two excess electrons reduce Mn in nearest-neighbor (NN) positions to the defect. Figure 3(c) schematically illustrates the changes in the Mn-O framework induced by the relaxations around an out-of-plane oxygen vacancy ($V_{O_{OP}}$). After breaking the two equivalent Mn-O_i bonds along the b axis, the structure relaxes by shortening the Mn-O_l bonds along c of the two undercoordinated NN Mn atoms [Mn_1 and Mn_5 in Fig. 3(c)] and significantly expanding the former Mn-O_s bonds of the next-nearest-neighbor (NNN) Mn atoms [Mn_4 and Mn_8 in Fig. 3(c)] along c. As a result of these relaxations, the energy of the d_{z^2} orbitals increases for Mn_1 and Mn_5 and decreases for Mn_4 and Mn_8 [see Fig. 3(d)], localizing the two excess electrons resulting from V_O formation on these orbitals and reducing the NNN Mn_4 and Mn_8 atoms [see Fig. 3(c)].

The case of an in-plane defect ($V_{O_{IP}}$), is more complex since both a Mn-O_s and a Mn-O_l bond are broken. As can be seen from Fig. 3(e), the structural relaxations upon $V_{O_{IP}}$ formation primarily involve one of the two NN Mn ions [Mn_5 and Mn_7 in Fig. 3(e) where a $V_{O_{IP}}$ created along the a axis is shown]. The NN Mn atom where a Mn-O_s bond was broken [Mn_5 in Fig. 3(e)] shortens its remaining Mn-O bonds along the c and b axes, resulting in elongated Mn-O bonds for NNN Mn sites around Mn_5: Mn_1 along b and Mn_8 along c [see Fig. 3(e)]. These bond-length changes are also reflected in the d_{z^2} and $d_{x^2-y^2}$ orbital energies of Mn_5 and Mn_7, respectively, that are increased due to breaking the Mn_5-O_{IP}-Mn_7 bond, while the $d_{x^2-y^2}$ and d_{z^2} orbitals of Mn_1 and Mn_8, respectively, are stabilized and filled by the excess electrons. Therefore also for the $V_{O_{IP}}$, the reduction happens on NNN Mn sites [see Figs. 3(e) and 3(f)].

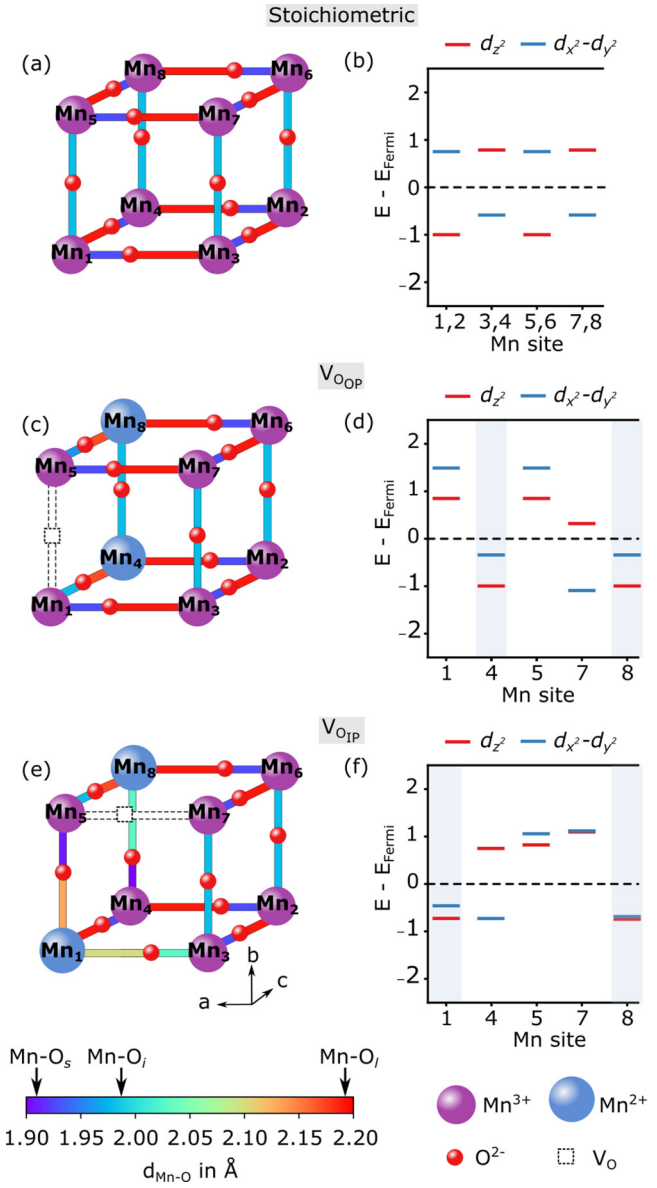

FIG. 3. Schematic representation of the Mn-O bond lengths (left) and energies of the d_{z^2} and $d_{x^2-y^2}$ orbitals for different Mn sites (right), determined as the centroid of the corresponding peaks in the atom- and orbital-resolved density of states. The horizontal dashed line indicates the Fermi energy. The shaded blue area indicates sites reduced upon V_O formation. Panels (a) and (b) for stoichiometric LMO, (c) and (d) for a $V_{O_{OP}}$, and (e) and (f) for a $V_{O_{IP}}$. Mn sites not shown in panels (d) and (f) are not noticeably affected by the defect.

For both vacancies, the reduced sites show almost equivalent Mn-O bond lengths (between 2.03 and 2.17 Å), in line with the fact that no JT distortion is expected for a Mn^{2+} ion (Mn' in Kröger-Vink notation [47]) in an octahedral crystal field. Furthermore, the average lengths of the Mn-O_s, Mn-O_i, and Mn-O_l bonds are 1.98, 2.17, and 2.20 Å in good agreement with the structural parameters reported by Hasteen *et al.* [23] for $LaMnO_{2.80}$ that has a V_O concentration very close to our calculations. Previous DFT calculations of oxygen vacancies in the high-temperature non-JT distorted *G*-AFM phase [49,50], reported reduction of the two NN Mn atoms, supporting that our findings stem from the JT distortion and orbital order in the *A*-AFM phase.

Interestingly, when the reduction does not take place on the Mn sites adjacent to the vacancy, the localization of the excess electrons with respect to the defect can be asymmetric and hence polar. We quantify this polarization considering the magnitude and orientation of the Mn'-$V_O^{\bullet\bullet}$ dipoles, identifying the reduced Mn sites based on structural changes and oxidation states calculated according to Ref. [51]. More details can be found in Supplemental Material [38] Sec. S1. For $V_{O_{OP}}$, a large polarization of 24.38 μC/cm^2 in the *ac* plane is observed while the out-of-plane contribution is zero, in line with the reduced Mn_4 and Mn_8, being symmetrically arranged with respect to the V_O along the *b* axis [Fig. 3(c)]. A polarization with in- and out-of-plane components of 17.08 and 10.20 μC/cm^2, respectively, is computed, instead, for the $V_{O_{IP}}$, in agreement with the larger asymmetry of the charge localization along the *b* axis. We note here that the local polarizations resulting from this novel mechanism are of similar magnitude as in conventional ferroelectrics such as $BaTiO_3$ as discussed in more detail in Supplemental Material [38] Sec. S1. We emphasize that the JT distortion is pivotal to obtain local polarizations of such magnitude. In non-JT distorted materials, vacancy formation on a Wyckoff position without an associated (local) inversion center can also result in a local dipole, the magnitude of which is, however, much smaller than in our case. With our model, we estimate a local polarization of only 3.6 μC/cm^2, assuming that the excess electrons localize on two Mn sites adjacent to the vacancy as in the non-JT-distorted *G*-AFM phase of LMO [49,50]. The key ingredient of our novel mechanisms is therefore the JT orbital-order induced excess charge localization on Mn atoms far from the oxygen vacancy, which together with the asymmetric charge arrangement yields the observed large local dipoles.

Different energetically equivalent patterns to accommodate the charges are possible. This is particularly apparent for the sketch in Fig. 3(c), where the charges are shown to localize on Mn sites along the positive *c* axis. Accommodation of charges on the Mn_4 and Mn_8 sites along the negative *c* axis, corresponds to an energetically equivalent situation, in which the local polarization, however, points in the opposite direction. For the $V_{O_{OP}}$ there are two such states, while for the $V_{O_{IP}}$ we expect four states, since equivalent positions exist along *b* for Mn_1 as well as along *c* for Mn_8. Given the high defect concentration achievable in experiment [22,23] it is conceivable that these local dipoles will couple, leading to an ordered ferroelectric phase. As such we expect the possibility of a switchable polarization that could lead to defect-induced ferroelectricity in reduced LMO.

Based on the preceding discussion, it is reasonable to expect that any external parameter affecting the Mn-O bond lengths and/or the orbital order will have a strong impact also on the charge localization and the resulting polarization. As one such external parameter, we investigate the effect of strain, both isostatic and biaxial, the latter induced, for example, by heteroepitaxial growth on a substrate with a different lattice parameter. As shown in Supplemental Material [38] Figs. S2 and S3, both types of strain are

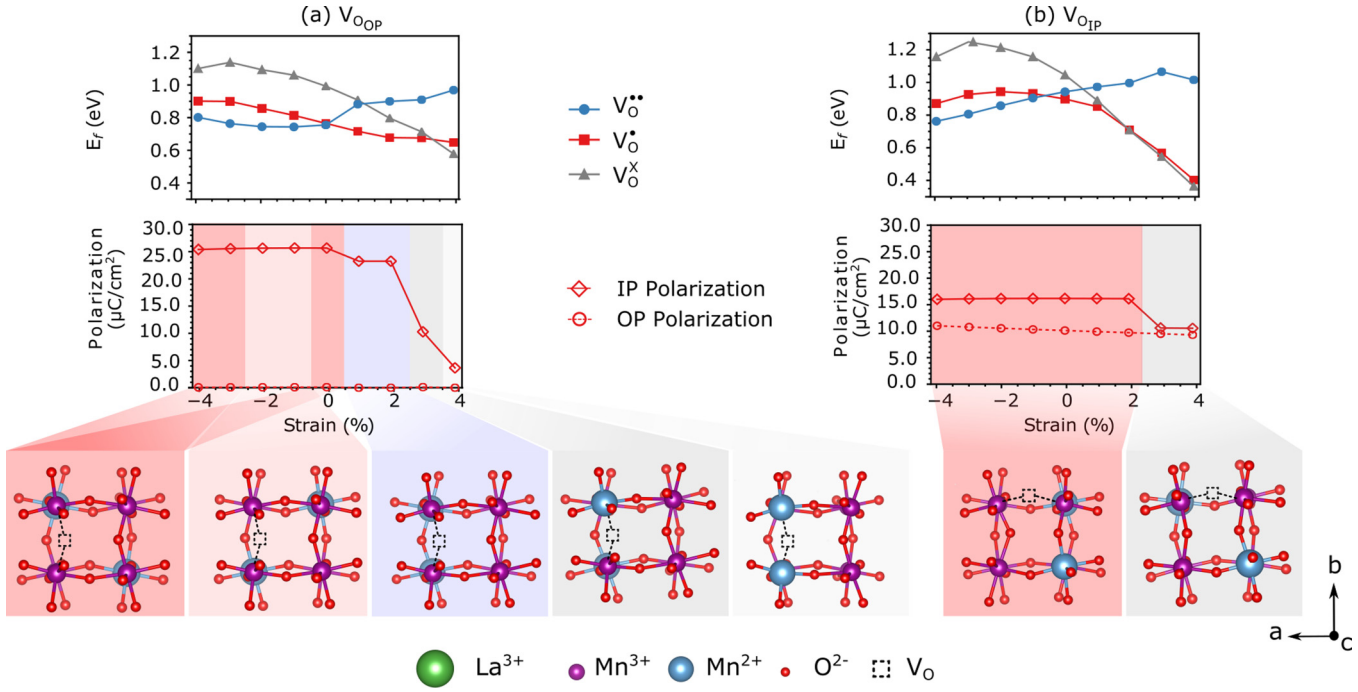

FIG. 4. Oxygen-vacancy formation energy [in the oxygen-poor limit, $\Delta\mu_O = -2.21$ eV and $E_F = 0.24$ eV; see Supplemental Material [38] Eq. (S1)] and polarization computed as a function of biaxial *ac* epitaxial strain for a neutral (a) $V_{O_{OP}}$ and (b) $V_{O_{IP}}$. The structures below the graphs illustrate the charge localization in the highlighted strain ranges.

accommodated in stoichiometric LMO by changes in octahedral tilt angles and bond lengths [52]. While Mn-O_s and Mn-O_i are relatively insensitive to strain, the Mn-O_l bonds are more strongly affected especially under tensile strain. This results in an increase of the JT mode amplitude Q_3 under tensile strain, while compressive strain reduces the Q_3 amplitude.

In Fig. 4 we show results for the formation energies, excess charge localization, and polarization under epitaxial strain. Results for isostatic strain are shown in Supplemental Material [38] Fig. S4. The localization of the excess charge away from the NN sites results in a strain dependence of the formation energy different from chemical expansion arguments [48,53,54] as discussed in Supplemental Material [38] Secs. S4–S6. While compressive strains favor neutral vacancies with slightly smaller formation energies for $V_{O_{OP}}$ than $V_{O_{IP}}$, tensile strain results in singly charged $V_{O_{OP}}$ and a mixture of singly and doubly charged $V_{O_{IP}}$, the latter not contributing to the local polarization due to the absence of excess charge. This implies that to obtain large polarizations, compressive strain seems more promising and that under these conditions neutral $V_{O_{OP}}$ will be predominantly stable, followed by neutral $V_{O_{IP}}$.

Epitaxial strain leads to changes in the excess-charge localization as a function of the strain magnitude. Interestingly, for both neutral $V_{O_{OP}}$ [(Fig. 4(a)] and $V_{O_{IP}}$ [Fig. 4(b)], imposing the constraint of a cubic substrate with equal *a* and *c* lattice parameters that result in the same *ac* area as bulk LMO (0% strain) induces a more asymmetric charge localization on NNN sites compared to the bulk. This excess-charge localization is maintained under compressive strain for both defects, with a slight variation for -1 and -2% strain for $V_{O_{OP}}$. This variation shows that energetically nearly degenerate excess-charge localization patterns exist. Under tensile strain, the excess charge localizes more symmetrically, for $V_{O_{OP}}$ first assuming the one of the bulk for 1 and 2% strain, before localizing one (for 3% strain) and then two (for 4% strain) of the excess electrons on NN Mn sites. For $V_{O_{IP}}$ the localization remains on NNN sites even for 4% tensile strain.

These strain-induced changes in charge localization affect also the local polarization, which depends on the relative arrangement of the two Mn'-$V_O^{\bullet\bullet}$ dipoles. For $V_{O_{OP}}$, the OP component of the polarization is almost zero throughout the whole investigated range of strains. The IP component reaches sizable values that depend on the excess charge localization pattern. For $V_{O_{IP}}$ the OP component is nonzero and fairly constant, while the IP component is significantly reduced for $+3$% and larger strain due to the change of the relative Mn' orientation in the *ac* plane. Similar results for less stable $V_O^{\bullet}$ are discussed in Supplemental Material [38] Sec. S5.

In summary, we have shown that, in the case of Jahn-Teller distorted perovskite oxides, the orbital order is an additional parameter to take into account during defect-based design of functional material properties. As we have shown for the example of oxygen vacancies in $LaMnO_3$, unexpected excess-charge localization results from the orbital order and can lead to the emergence of local polarization. The charge localization and hence the polarization magnitude are tunable by strain, suggesting the possibility to engineer ferroelectricity in $LaMnO_3$ when local dipoles couple for high enough, yet experimentally attainable, defect concentrations.

This research was supported by the NCCR MARVEL, funded by the Swiss National Science Foundation. Computational resources were provided by the University of Bern (on the HPC cluster UBELIX [55]), by the Swiss National Supercomputing Center (CSCS) under projects ID mr26 and SuperMUC at GCS@LRZ, Germany, for which we acknowledge PRACE for awarding us access.

[1] S. Jin, T. H. Tiefel, M. McCormack, R. A. Fastnacht, R. Ramesh, and L. H. Chen, Thousandfold change in resistivity in magnetoresistive La-Ca-Mn-O films, Science **264**, 413 (1994).

[2] P. Schiffer, A. P. Ramirez, W. Bao, and S.-W. Cheong, Low Temperature Magnetoresistance and the Magnetic Phase Diagram of $La_{1-x}Ca_xMnO_3$, Phys. Rev. Lett. **75**, 3336 (1995).

[3] A. J. Millis, Lattice effects in magnetoresistive manganese perovskites, Nature (London) **392**, 147 (1998).

[4] J. M. D. Coey, M. Viret, and S. von Molnár, Mixed-valence manganites, Adv. Phys. **48**, 167 (1999).

[5] H. Yamada, Y. Ogawa, Y. Ishii, H. Sato, M. Kawasaki, H. Akoh, and Y. Tokura, Engineered interface of magnetic oxides, Science **305**, 646 (2004).

[6] T. Mertelj, D. Kuščer, M. Kosec, and D. Mihailovic, Photoinduced infrared absorption in $(La_{1-x}Sr_xMn)_{1-\delta}O_3$: Changes of the small polaron binding energy with doping, Phys. Rev. B **61**, 15102 (2000).

[7] S. P. Jiang, Development of lanthanum strontium manganite perovskite cathode materials of solid oxide fuel cells: A review, J. Mater. Sci. **43**, 6799 (2008).

[8] E. Dagotto, Complexity in strongly correlated electronic systems, Science **309**, 257 (2005).

[9] S.-W. Cheong, Transition metal oxides: The exciting world of orbitals, Nat. Mater. **6**, 927 (2007).

[10] I. Loa, P. Adler, A. Grzechnik, K. Syassen, U. Schwarz, M. Hanfland, G. Kh. Rozenberg, P. Gorodetsky, and M. P. Pasternak, Pressure-Induced Quenching of the Jahn-Teller Distortion and Insulator-to-Metal Transition in $LaMnO_3$, Phys. Rev. Lett. **87**, 125501 (2001).

[11] P. Mondal, D. Bhattacharya, P. Choudhury, and P. Mandal, Dielectric anomaly at T_N in $LaMnO_3$ as a signature of coupling between spin and orbital degrees of freedom, Phys. Rev. B **76**, 172403 (2007).

[12] D. Muñoz, N. M. Harrison, and F. Illas, Electronic and magnetic structure of $LaMnO_3$ from hybrid periodic density-functional theory, Phys. Rev. B **69**, 085115 (2004).

[13] J. H. Lee, K. T. Delaney, E. Bousquet, N. A. Spaldin, and K. M. Rabe, Strong coupling of Jahn-Teller distortion to oxygen-octahedron rotation and functional properties in epitaxially strained orthorhombic $LaMnO_3$, Phys. Rev. B **88**, 174426 (2013).

[14] C. Ritter, M. R. Ibarra, J. M. De Teresa, P. A. Algarabel, C. Marquina, J. Blasco, J. García, S. Oseroff, and S.-W. Cheong, Influence of oxygen content on the structural, magnetotransport, and magnetic properties of $LaMnO_{3+\delta}$, Phys. Rev. B **56**, 8902 (1997).

[15] P. Norby, I. G. Krogh Andersen, E. Krogh Andersen, and N. H. Andersen, The crystal structure of lanthanum manganate(iii), $LaMnO_3$, at room temperature and at 1273 K under N_2, J. Solid State Chem. **119**, 191 (1995).

[16] J. Rodríguez-Carvajal, M. Hennion, F. Moussa, A. H. Moudden, L. Pinsard, and A. Revcolevschi, Neutron-diffraction study of the Jahn-Teller transition in stoichiometric $LaMnO_3$, Phys. Rev. B **57**, R3189 (1998).

[17] X. Qiu, Th. Proffen, J. F. Mitchell, and S. J. L. Billinge, Orbital Correlations in the Pseudocubic O and Rhombohedral R Phases of $LaMnO_3$, Phys. Rev. Lett. **94**, 177203 (2005).

[18] J. A. M. Van Roosmalen and E. H. P. Cordfunke, The defect chemistry of $LaMnO_{3\pm\delta}$: 3. The density of $(La,A)MnO_{3\pm\delta}$ (A = Ca, Sr, Ba), J. Solid State Chem. **110**, 106 (1994).

[19] J. Töpfer and J. B. Goodenough, $LaMnO_{3+\delta}$ revisited, J. Solid State Chem. **130**, 117 (1997).

[20] L. Ghivelder, I. A. Castillo, M. A. Gusmão, J. A. Alonso, and L. F. Cohen, Specific heat and magnetic order in $LaMnO_{3+\delta}$, Phys. Rev. B **60**, 12184 (1999).

[21] R. Laiho, K. G. Lisunov, E. Lähderanta, P. A. Petrenko, J. Salminen, V. N. Stamov, Yu. P. Stepanov, and V. S. Zakhvalinskii, Low-field magnetic properties of $LaMnO_{3+\delta}$ with $0.065 \leqslant \delta \leqslant 0.154$, J. Phys. Chem. Solids **64**, 2313 (2003).

[22] F. Abbattista and M. Lucco Borlera, Reduction of $LaMnO_3$. Structural features of phases $La_8Mn_8O_{23}$ and $La_4Mn_4O_{11}$, Ceram. Int. **7**, 137 (1981).

[23] O. H. Hansteen, Y. Bréard, H. Fjellvåg, and B. C. Hauback, Divalent manganese in reduced $LaMnO_{3-\delta}$—Effect of oxygen nonstoichiometry on structural and magnetic properties, Solid State Sci. **6**, 279 (2004).

[24] A. Gupta, T. R. McGuire, P. R. Duncombe, M. Rupp, J. Z. Sun, W. J. Gallagher, and G. Xiao, Growth and giant magnetoresistance properties of La-deficient $LaMnO_{3-\delta}$ ($0.67 \leqslant x \leqslant 1$) films, Appl. Phys. Lett. **67**, 3494 (1995).

[25] P. Murugavel, J. H. Lee, J.-G. Yoon, T. W. Noh, J.-S. Chung, M. Heu, and S. Yoon, Origin of metal-insulator transition temperature enhancement in underdoped lanthanum manganite films, Appl. Phys. Lett. **82**, 1908 (2003).

[26] S. Smadici, P. Abbamonte, A. Bhattacharya, X. Zhai, B. Jiang, A. Rusydi, J. N. Eckstein, S. D. Bader, and J.-M. Zuo, Electronic Reconstruction at $SrMnO_3$-$LaMnO_3$ Superlattice Interfaces, Phys. Rev. Lett. **99**, 196404 (2007).

[27] C. Aruta, M. Angeloni, G. Balestrino, N. G. Boggio, P. G. Medaglia, A. Tebano, B. Davidson, M. Baldini, D. Di Castro, P. Postorino *et al.*, Preparation and characterization of $LaMnO_3$ thin films grown by pulsed laser deposition, J. Appl. Phys. **100**, 023910 (2006).

[28] J. Garcia-Barriocanal, F. Y. Bruno, A. Rivera-Calzada, Z. Sefrioui, R. M. Nemes, M. Garcia-Hernández, J. Rubio-Zuazo, G. R. Castro, M. Varela, S. J. Pennycook *et al.*, "Charge leakage" at $LaMnO_3$/$SrTiO_3$ interfaces, Adv. Mater. **22**, 627 (2010).

[29] A. B. Shah, Q. M. Ramasse, X. Zhai, J. G. Wen, S. J. May, I. Petrov, A. Bhattacharya, P. Abbamonte, J. N. Eckstein, and J.-M. Zuo, Probing interfacial electronic structures in atomic layer $LaMnO_3$ and $SrTiO_3$ superlattices, Adv. Mater. **22**, 1156 (2010).

[30] R. Zhao, K. Jin, Z. Xu, H. Guo, L. Wang, C. Ge, H. Lu, and G. Yang, The oxygen vacancy effect on the magnetic property of the $LaMnO_{3-\delta}$ thin films, Appl. Phys. Lett. **102**, 122402 (2013).

[31] Y. K. Liu, H. F. Wong, K. K. Lam, C. L. Mak, and C. W. Leung, Tuning ferromagnetic properties of $LaMnO_3$ films by oxygen vacancies and strain, J. Magn. Magn. Mater. **481**, 85 (2019).

[32] X. Renshaw Wang, C. J Li, W. M. Lü, T. R. Paudel, D. P. Leusink, M Hoek, N Poccia, A Vailionis, T. Venkatesan, J. M. D. Coey *et al.*, Imaging and control of ferromagnetism in $LaMnO_3/SrTiO_3$ heterostructures, Science **349**, 716 (2015).

[33] H. S. Kim and H. M. Christen, Controlling the magnetic properties of $LaMnO_3$ thin films on $SrTiO_3(100)$ by deposition in a O_2/Ar gas mixture, J. Phys.: Condens. Matter **22**, 146007 (2010).

[34] J. Roqueta, A. Pomar, L. Balcells, C. Frontera, S. Valencia, R. Abrudan, B. Bozzo, Z. Konstantinović, J. Santiso, and B. Martínez, Strain-engineered ferromagnetism in $LaMnO_3$ thin films, Cryst. Growth Des. **15**, 5332 (2015).

[35] W. S. Choi, Z. Marton, S. Y. Jang, S. J. Moon, B. C. Jeon, J. H. Shin, S. S. A. Seo, T. W. Noh, K. Myung-Whun, H. N. Lee, and Y. S. Lee, Effects of oxygen-reducing atmosphere annealing on $LaMnO_3$ epitaxial thin films, J. Phys. D: Appl. Phys. **42**, 165401 (2009).

[36] P. Giannozzi, S. Baroni, N. Bonini, M. Calandra, R. Car, C. Cavazzoni, D. Ceresoli, G. L. Chiarotti, M. Cococcioni, I. Dabo *et al.*, QUANTUM ESPRESSO: A modular and open-source software project for quantum simulations of materials, J. Phys.: Condens. Matter **21**, 395502 (2009).

[37] P. Giannozzi, O. Andreussi, T. Brumme, O. Bunau, M. Buongiorno Nardelli, M. Calandra, R. Car, C. Cavazzoni, D. Ceresoli, M. Cococcioni *et al.*, Advanced capabilities for materials modelling with QUANTUM ESPRESSO, J. Phys.: Condens. Matter **29**, 465901 (2017).

[38] See Supplemental Material at http://link.aps.org/supplemental/10.1103/PhysRevResearch.2.042040 for computational details, electronic structure information, and isostatic strain effects.

[39] J. P. Perdew, A. Ruzsinszky, G. I. Csonka, O. A. Vydrov, G. E. Scuseria, L. A. Constantin, X. Zhou, and K. Burke, Restoring the Density-Gradient Expansion for Exchange in Solids and Surfaces, Phys. Rev. Lett. **100**, 136406 (2008).

[40] S. L. Dudarev, G. A. Botton, S. Y. Savrasov, C. J. Humphreys, and A. P. Sutton, Electron-energy-loss spectra and the structural stability of nickel oxide: An LSDA+U study, Phys. Rev. B **57**, 1505 (1998).

[41] I. Timrov, N. Marzari, and M. Cococcioni, Hubbard parameters from density-functional perturbation theory, Phys. Rev. B **98**, 085127 (2018).

[42] C. Ricca, I. Timrov, M. Cococcioni, N. Marzari, and U. Aschauer, Self-consistent site-dependent DFT+U study of stoichiometric and defective $SrMnO_3$, Phys. Rev. B **99**, 094102 (2019).

[43] T. Hashimoto, S. Ishibashi, and K. Terakura, Jahn-Teller distortion and magnetic structure in $LaMnO_3$: A first-principles theoretical study with full structure optimizations, Phys. Rev. B **82**, 045124 (2010).

[44] J. He and C. Franchini, Screened hybrid functional applied to $3d^0 \rightarrow 3d^8$ transition-metal perovskites $LaMO_3$ (M = Sc-Cu): Influence of the exchange mixing parameter on the structural, electronic, and magnetic properties, Phys. Rev. B **86**, 235117 (2012).

[45] A. L. Gavin and G. W. Watson, Modelling the electronic structure of orthorhombic $LaMnO_3$, Solid State Ionics **299**, 13 (2017).

[46] R. Mahendiran, A. K. Raychaudhuri, A. Chainani, D. D. Sarma, and S. B. Roy, Large magnetoresistance in $La_{1-x}Sr_xMnO_3$ and its dependence on magnetization, Appl. Phys. Lett. **66**, 233 (1995).

[47] F. A. Kröger and H. J. Vink, Relations between the concentrations of imperfections in crystalline solids, Solid State Phys. **3**, 307 (1956).

[48] U. Aschauer, R. Pfenninger, S. M. Selbach, T. Grande, and N. A. Spaldin, Strain-controlled oxygen vacancy formation and ordering in $CaMnO_3$, Phys. Rev. B **88**, 054111 (2013).

[49] M. Pavone, A. B. Muñoz-García, A. M. Ritzmann, and E. A. Carter, First-principles study of lanthanum strontium manganite: Insights into electronic structure and oxygen vacancy formation, J. Phys. Chem. C **118**, 13346 (2014).

[50] E. Olsson, X. Aparicio-Anglès, and N. H. de Leeuw, Ab initio study of vacancy formation in cubic $LaMnO_3$ and $SmCoO_3$ as cathode materials in solid oxide fuel cells, J. Chem. Phys. **145**, 014703 (2016).

[51] P. H.-L. Sit, R. Car, M. H. Cohen, and A. Selloni, Simple, unambiguous theoretical approach to oxidation state determination via first-principles calculations, Inorg. Chem. **50**, 10259 (2011).

[52] J. M. Rondinelli and N. A. Spaldin, Structure and properties of functional oxide thin films: Insights from electronic-structure calculations, Adv. Mater. **23**, 3363 (2011).

[53] S. B. Adler, Chemical expansivity of electrochemical ceramics, J. Am. Ceram. Soc. **84**, 2117 (2001).

[54] U. Aschauer and N. A. Spaldin, Interplay between strain, defect charge state, and functionality in complex oxides, Appl. Phys. Lett. **109**, 031901 (2016).

[55] http://www.id.unibe.ch/hpc.